Chromosomal passenger complex hydrodynamics suggests chaperoning of the inactive state by nucleoplasmin/nucleophosmin

Mariah L. Hanley[a,b], Tae Yeon Yoo[c], Matthew Sonnett[a], Daniel J. Needleman[c,d], and Timothy J. Mitchison[a,*]

[a]Department of Systems Biology, Harvard Medical School, Boston, MA 02114–5701; [b]Department of Chemistry, [c]John A. Paulson School of Engineering and Applied Sciences, and [d]Department of Molecular and Cellular Biology, Harvard University, Cambridge, MA 02138-2902

ABSTRACT **The chromosomal passenger complex (CPC) is a conserved, essential regulator of cell division. As such, significant anti–cancer drug development efforts have been focused on targeting it, most notably by inhibiting its AURKB kinase subunit. The CPC is activated by AURKB-catalyzed autophosphorylation on multiple subunits, but how this regulates CPC interactions with other mitotic proteins remains unclear. We investigated the hydrodynamic behavior of the CPC in *Xenopus laevis* egg cytosol using sucrose gradient sedimentation and in HeLa cells using fluorescence correlation spectroscopy. We found that autophosphorylation of the CPC decreases its sedimentation coefficient in egg cytosol and increases its diffusion coefficient in live cells, indicating a decrease in mass. Using immunoprecipitation coupled with mass spectrometry and immunoblots, we discovered that inactive, unphosphorylated CPC interacts with nucleophosmin/nucleoplasmin proteins, which are known to oligomerize into pentamers and decamers. Autophosphorylation of the CPC causes it to dissociate from nucleophosmin/nucleoplasmin. We propose that nucleophosmin/nucleoplasmin complexes serve as chaperones that negatively regulate the CPC and/or stabilize its inactive form, preventing CPC autophosphorylation and recruitment to chromatin and microtubules in mitosis.**

Monitoring Editor
Yixian Zheng
Carnegie Institution

Received: Dec 20, 2016
Revised: Mar 27, 2017
Accepted: Apr 4, 2017

This article was published online ahead of print in MBoC in Press (http://www.molbiolcell.org/cgi/doi/10.1091/mbc.E16-12-0860) on April 12, 2017.

The authors declare that they have no conflicts of interest with regard to this article.

M.L.H. and T.J.M. designed the study. M.L.H. performed all experiments unless otherwise noted. T.Y.Y. performed FCS experiments, and T.T.Y. and D.J.N. analyzed the results. M.L.H. and M.S. performed and analyzed IP-MS experiments. M.L.H. and T.J.M. wrote the manuscript, with assistance in figure preparation from T.Y.Y. T.J.M. and D.J.N. provided funding. All authors reviewed the results and approved the final version of the manuscript.

*Address correspondence to: Timothy J. Mitchison (timothy_mitchison@hms.harvard.edu).

Abbreviations used: AURKB, AuroraB kinase; BAC, bacterial artificial chromosome; BIRC5, survivin; CDCA8, borealin/DasraB; CDCA9, DasraA; CDK, cyclin-dependent kinase; CPC, chromosomal passenger complex; CRISPR/Cas9, clustered regularly interspaced short palindromic repeats/Cas9 DNA endonuclease; FCS, fluorescence correlation spectroscopy; HSS, high-speed supernatant of *Xenopus laevis* egg extract; INCENP, inner centromere protein; MPM2, mitotic protein 2; NPM, nucleophosmin (NPM1) or nucleoplasmin (NPM2); OA, okadaic acid; PARD3, partitioning defective 3 homologue; STLC, *S*-trityl-L-cysteine; STMN, stathmin/Op18; S-value, sedimentation coefficient; TMT, tandem mass tags.

INTRODUCTION

The four-protein chromosomal passenger complex (CPC) is essential for proper cell division in many eukaryotes (Sampath *et al.*, 2004; Nguyen *et al.*, 2014). Comprising one each of AuroraB kinase (AURKB), inner centromere protein (INCENP), borealin/DasraB (CDCA8), and survivin (BIRC5) subunits, the complex localizes to mitotic chromosomes during metaphase, where it is involved in chromosome condensation (Mackay *et al.*, 1998) and the spindle assembly checkpoint (Tseng *et al.*, 2010). During anaphase and cytokinesis, the CPC redistributes to the midzone between microtubule asters, where it assists in localizing the cleavage furrow and triggering its ingression (Cooke *et al.*, 1987; Field *et al.*, 2015).

The CPC and its individual subunits have been extensively studied both to understand their biological function and to investigate AURKB as a potential drug target for cancer treatment (Portella *et al.*, 2011). AURKB is a critical mitotic kinase that phosphorylates many mitotic proteins (Carmena *et al.*, 2012), including the CPC components INCENP (Adams *et al.*, 2000; Bishop and Schumacher, 2002; Honda *et al.*, 2003; Sessa *et al.*, 2005) and CDCA8 (Gassmann *et al.*, 2004). AURKB also phosphorylates itself on Thr-232 within its activation loop (Yasui *et al.*, 2004). Clustering the CPC on chromatin

or microtubules or multimerizing it with antibodies triggers activating autophosphorylation of AURKB, suggesting that this occurs in-*trans* (Kelly *et al.*, 2007). In addition, AURKB phosphorylation of INCENP allosterically activates AURKB (Adams *et al.*, 2000; Bishop and Schumacher, 2002; Honda *et al.*, 2003; Sessa *et al.*, 2005). Despite this progress, we lack full understanding of how the CPC is regulated by autophosphorylation.

Crystal structures of both termini of INCENP and its CPC binding partners have been obtained, but the structure of the entire complex remains elusive (Sessa *et al.*, 2005; Jeyaprakash *et al.*, 2007; Sessa and Villa, 2014). The middle region of INCENP was previously believed to contain a coiled-coil domain, but recent evidence suggests that this region may in fact be a single α-helix 32 nm long that is capable of stretching up to 80 nm, allowing CDCA8 and BIRC5 to anchor the complex while AURKB phosphorylates other proteins in the vicinity (Samejima *et al.*, 2015). A long, single α-helix may be prone to degradation and might need to be stabilized when the complex is inactive. Inactive CPC is unphosphorylated on key residues of AURKB and INCENP, but whether posttranslational modifications or chaperone proteins assist in stabilizing the inactive state is unknown. Stabilization of an inactive state by these mechanisms is common in other kinases (Shalloway and Taylor, 1997), other cytokinesis proteins (Staus *et al.*, 2011), and other protein complexes (Berrabah *et al.*, 2011; Koryakina *et al.*, 2014).

Hydrodynamic measurements provide a classic approach to elucidating regulatory mechanisms of protein complexes. Comparison of the CPC sedimentation coefficient in interphase and mitotic *Xenopus laevis* extracts revealed slower sedimentation rate in mitosis, which was attributed to cell cycle regulation (Bolton *et al.*, 2002). However, in that study, the mitotic extract was treated with the phosphatase inhibitor microcystin and diluted into buffer containing additional phosphatase inhibitors, whereas the interphase extract was not treated with phosphatase inhibitors at any step. Therefore the reported difference in sedimentation coefficient between mitotic and interphase CPC could have been caused by artificial induction of CPC autophosphorylation and activation in the mitotic sample rather than by the cell cycle state difference. Here we show that autophosphorylation does indeed determine CPC's sedimentation coefficient in both mitosis and interphase, and we use the resulting hydrodynamic information to gain additional insights into how the CPC is regulated.

The *X. laevis* egg extract system is ideal for studying the CPC, as it is arrested in a mitotic state and contains a relatively high concentration of CPC proteins (estimated between 55 and 155 nM, based on mass spectrometry of individual subunits; Wuhr *et al.*, 2014). *X. laevis* has different maternally stored and embryonically expressed forms of CDCA8 and BIRC5; we will refer to the maternally stored forms analyzed in this work as CDCA9 (also known as DasraA) and BIRC5.1, respectively. Here we use high-speed supernatant (HSS) of *X. laevis* egg extract lacking glycogen or membranous organelles prepared such that the cell cycle state (mitotic or interphase) was retained (Groen *et al.*, 2011; Mitchison *et al.*, 2013). In particular, a degradation-resistant form of cyclin B was added to the extract before the high-speed spin to stabilize the mitotic state of HSS without the use of phosphatase inhibitors. A major downside to the *X. laevis* extract system is its lack of genetic tractability, which makes tagging of endogenous proteins with green fluorescent protein (GFP) variants difficult. We therefore also investigated CPC behavior in mitotic HeLa cells, using the clustered regularly interspaced short palindromic repeats/Cas9 DNA endonuclease (CRISPR/Cas9) system to tag endogenous proteins with GFP (Cong *et al.*, 2013). Although CPC protein sequences vary between the *X. laevis* and *Homo sapiens* (ranging from 70% identical for AURKB to only 24% for CDCA8/9; see *Materials and Methods*), the overall architecture and regulation of the complex are highly conserved.

We report that the CPC hydrodynamic profile changes with autophosphorylation regardless of cell cycle state. This change occurs in both *X. laevis* extract and live mitotic HeLa cells and indicates a decrease in native molecular weight upon activation. We then provide evidence for an interaction between the CPC in its inactive state and the nucleophosmin/nucleoplasmin (NPM) family of oligomeric histone chaperones. We propose that NPM complexes are regulatory chaperones that stabilize the inactive state of the CPC.

RESULTS

CPC autophosphorylation causes a decrease in sedimentation coefficient

Human AURKB is controlled in part by autophosphorylation on T232 in its activation loop, which activates the kinase (Yasui *et al.*, 2004). To examine phosphoregulation of *X. laevis* AURKB and the CPC as a whole, we used a phosphatase inhibitor, okadaic acid, in combination with AURKB inhibitors (barasertib, ZM447439, and VX680, listed here from most to least specific) in a variety of applications. We first wanted to confirm that autophosphorylation of this site occurs in mitotic *X. laevis* HSS (clarified extract from eggs; Groen *et al.*, 2011). We incubated HSS with AURKB inhibitors, okadaic acid, or sequential treatment with AURKB inhibitors, followed by okadaic acid. AURKB phosphosites will be blocked from phosphorylation by pretreatment with AURKB inhibitors, but all other phosphosites will become phosphorylated in response to okadaic acid. We performed immunoblot analysis of the treated extracts for pThr232-AURKB, and stathmin/Op18 (STMN), a known AURKB target that undergoes a gel shift upon phosphorylation (Gadea and Ruderman, 2006). The pThr232-AURKB antibody was raised to the activation-loop phosphosite in humans with high homology in *X. laevis* AURKA and AURKB (Figure 1A). As anticipated, okadaic acid addition promoted AURKB and STMN phosphorylation, as shown by a band shift in the latter protein (Figure 1B). These phosphorylations were blocked by pretreatment with AURKB inhibitors, indicating that AURKB and STMN phosphorylation requires AURKB activity in mitotic HSS. Diluting HSS before adding okadaic acid reduced AURKB phosphorylation (Supplemental Figure S2), suggesting that two CPCs may interact to promote AURKB phosphorylation in-*trans*, which is consistent with prior reports (Kelly *et al.*, 2007).

Using the drug treatments characterized in Figure 1B, we probed the hydrodynamic properties of the CPC in mitotic HSS as a function of its activity state. After drug treatment, we diluted HSS 1:1 in S-CSF-XB-phosphate, fractionated it on 5–40% sucrose gradients, and blotted fractions with antibodies raised against *X. laevis* INCENP and CDCA9 (Figure 1C, top; Sampath *et al.*, 2004). In all cases, INCENP and CDCA9 cofractionated, suggesting that the complex stays intact during centrifugation. There was no difference in sedimentation between basal state of mitotic HSS and HSS preincubated with barasertib, a highly specific AURKB inhibitor. However, when mitotic HSS was preincubated with okadaic acid, the CPC proteins sedimented substantially higher up on the sucrose gradient (Figure 1C, second bracket from bottom). The shift in sedimentation coefficient (S-value) is similar to that previously observed based on bovine serum albumin (BSA; 4S) and bovine γ-globulin (7S) standards run on a parallel gradient (Bolton *et al.*, 2002). This shift could be due to a decrease in mass upon phosphorylation or to a conformational change to a more extended conformation with a higher frictional coefficient.

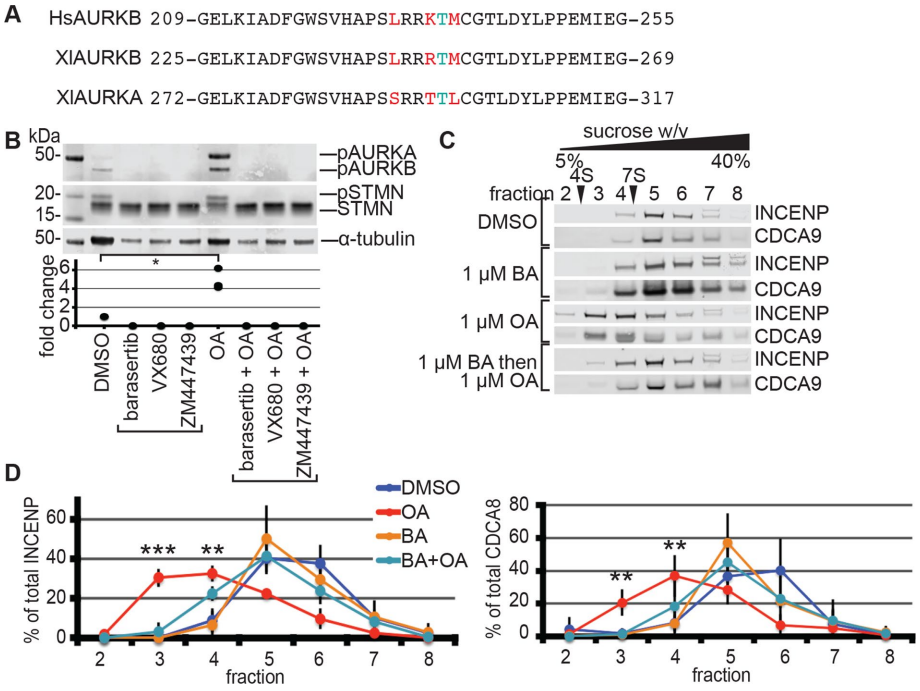

FIGURE 1: Phosphatase inhibition activates AURKB and causes a change in the hydrodynamic properties of its associated protein complex. (A) Sequences of the activation loop of human and *X. laevis* AURKB and *X. laevis* AURKA. Differences are highlighted in red, and the key phosphorylated threonine is highlighted in turquoise. (B) Mitotic HSS was incubated with kinase inhibitors and okadaic acid. Equal reaction volumes were run on an SDS–PAGE gel and immunoblotted with antibodies against pT232-AURK (which recognizes AURKA, AURKB, and AURKC phosphorylated at the conserved threonine on the activation loop of the kinase), STMN, and α-tubulin. The blot was quantified by normalizing pAURKB intensity to α-tubulin intensity and set such that the lowest value of each replicate was the DMSO control (lanes where no intensity could be detected are marked as zero). The *p* value between the DMSO and okadaic acid samples is 0.014; $n = 3$. (C) Mitotic HSS was incubated with kinase inhibitor or DMSO for 25 min, followed by okadaic acid or DMSO for an additional 25 min. Equal volumes were sedimented on 5–40% sucrose gradients for 6 h at 237,000 × *g* and 4°C. The indicated fractions were separated on SDS–PAGE gels and immunoblotted with antibodies against INCENP and CDCA9. The identity of the higher–molecular weight band in higher-numbered INCENP blots is unknown but likely corresponds to a posttranslationally modified version of INCENP. Full blots with molecular weight markers are given in Supplemental Figure S1. (D) Sucrose gradient blots in C were quantified and normalized to the total amount of the indicated protein in the gradient. Error bars represent SD. The *p* values indicated by asterisks were calculated between the barasertib- and okadaic acid–treated samples in fractions 3 (INCENP 0.00046, CDCA9 0.0075) and 4 (INCENP 0.0057, CDCA9 0.0062); $n = 4$.

To test whether AURKB activity is necessary for the observed phosphorylation-induced hydrodynamic shift of the CPC, we used the same two-drug strategy as in Figure 1B, sequentially dosing with barasertib and okadaic acid, followed by sucrose gradient sedimentation. The CPC proteins had the same S-value as in the basal and AURKB-inhibited states (Figure 1C, bottom). Therefore AURKB activity is required to reduce the value of the sedimentation coefficient of the CPC in response to okadaic acid treatment.

CPC sedimentation behavior is not primarily regulated by the cell cycle state

Similar basal hydrodynamic properties of the CPC in *X. laevis* were previously reported, and a shift from high- to low-S form was attributed to cell cycle regulation (Bolton *et al.*, 2002). In those experiments, a phosphatase inhibitor was added to mitotic but not interphase samples, so it is possible that the observed S-value shifts were instead due to phosphorylation effects, as we observed in Figure 1C. The mitotic HSS used in Figure 1 was prepared using methods that do not require phosphatase inhibitors to stabilize the mitotic state by adding recombinant cyclin B Δ90 to the crude extract before centrifugation (Groen *et al.*, 2011). To test the effect of cell cycle on CPC hydrodynamic behavior and AURKB phosphorylation, we prepared interphase HSS by first cycling crude mitotic extract into interphase with the addition of calcium and then preventing any further protein translation with the addition of cycloheximide before the centrifugation step that transforms crude extract into HSS. To confirm the cell cycle state of mitotic and interphase HSS, we immunoblotted with an antibody against phosphorylated epitopes of mitotic protein 2 (MPM2) target sites, which are more abundant in mitosis (Figure 2A; Kuang *et al.*, 1994; Field *et al.*, 2014). Substantially less protein phosphorylated by MPM2 was recognized in the interphase than in the mitotic sample, showing that the cell cycle state had been maintained throughout the HSS preparation without the use of phosphatase inhibitors. Similar to MPM2, band intensity ratios between interphase and mitotic crude extract were previously reported by Field *et al.* (2011) and are shown in Supplemental Figure S4A.

We repeated the sucrose gradient experiments to probe the effects of kinase and phosphatase inhibitors on the CPC, comparing interphase and mitotic HSS prepared from the same extract. Treatment with 1 μM okadaic acid was sufficient to shift mitotic CPC to the low-S form, but 10 μM was required to shift interphase CPC (Figure 2, B and C). We therefore concluded that the basal state of the CPC is the same in both cell cycle states and can undergo similar phosphorylation-driven shifts to the lower-S form, although less phosphatase inhibition is required in mitosis. We next tested the levels of AURKB phosphorylation at Thr-232 in response to inhibitors (Figure 2D). Unsurprisingly, AURKB phosphorylation was promoted by okadaic acid and inhibited by barasertib in both cell cycle states. We concluded that autophosphorylation drives the CPC to a lower S-value independent of cell cycle state.

We attempted to measure the Stokes radius of the native and phosphorylated CPC using gel filtration chromatography to compare changes in size with the hydrodynamic behavior observed on sucrose gradients. However, during gel filtration in a wide range of buffers and on a wide range of resins, the CPC smeared out on the column. Blots of the fractions for CPC subunits suggested that the complex dissociated, potentially in response to dilution or to nonspecific interactions with the resin. Similar results were seen in a previous study (Bolton *et al.*, 2002). We therefore turned to a less perturbing method, fluorescence correlation spectroscopy (FCS), to further probe CPC hydrodynamics (see later description).

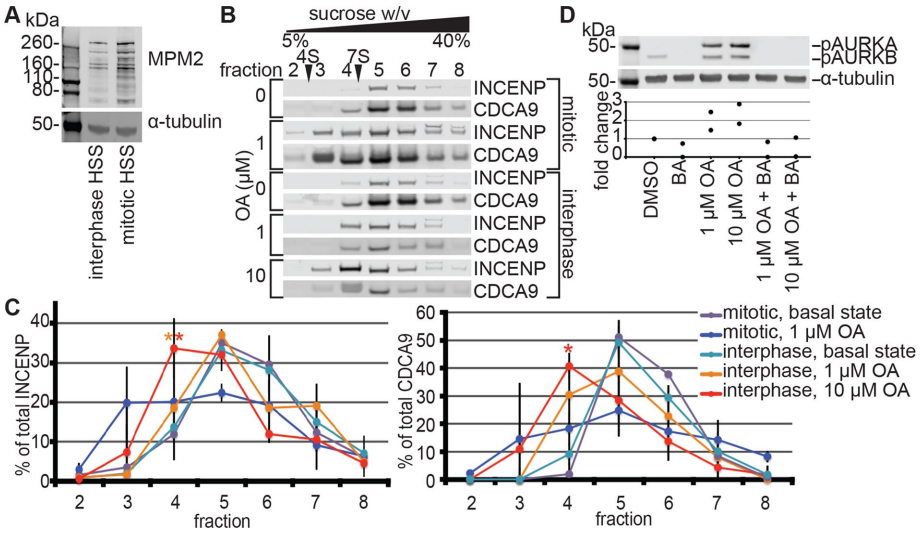

FIGURE 2: CPC hydrodynamic properties are similar in interphase and mitotic HSS. (A) Interphase HSS was prepared by cycling CSF *X. laevis* egg extract into interphase with calcium and then adding cycloheximide, followed by the high-speed spin. Equal amounts of interphase and mitotic HSS prepared from the same extract were blotted with an MPM2 (mitotic phosphoprotein monoclonal) antibody that recognizes many CDK1 phosphosites more prevalent in mitosis (Kuang *et al.*, 1994; Field *et al.*, 2014). Interphase extract was prepared more than five times and compared with mitotic HSS prepared from the same crude extract using MPM2 blots twice. (B) Sucrose gradients were run as in Figure 1. Mitotic and interphase HSS were prepared from the same extract. Fractions were immunoblotted with antibodies raised against INCENP and CDCA9 after SDS–PAGE. Full blots with molecular weight markers are given in Supplemental Figure S3. (C) Sucrose gradient blots from B were quantified as in Figure 1D. Error bars represent SD; $n = 2$. For fraction 4, significant p values comparing basal interphase HSS and interphase HSS dosed with 1 and 10 μM okadaic acid (OA) were calculated to be 0.011 (INCENP, 1 μM OA), 0.050 (INCENP, 10 μM OA), and 0.014 (CDCA9, 10 μM OA); $n = 2$–5. (D) Mitotic and interphase HSS samples prepared from the same extract were incubated with the indicated drugs as in Figure 1. The reactions were then blotted with antibodies against pT232-AURKB and α-tubulin, and pAURKB levels were quantified by normalizing to α-tubulin; $n = 2$.

Activation of soluble CPC causes faster diffusion in live HeLa cells

We next investigated whether hydrodynamic regulation of the CPC also occurs in human cells. To test whether CPC autophosphorylation can be triggered by okadaic acid in HeLa cells, we synchronized cells in mitosis by overnight treatment with the kinesin-5 inhibitor *S*-trityl-L-cysteine (STLC; Hu *et al.*, 2012). This arrests cells in monopolar mitosis while minimally perturbing microtubule dynamics. We then incubated with barasertib, okadaic acid, or both drugs concurrently and lysed cells with SDS–PAGE running buffer. We then blotted with the antibody against pThr232-AURKB used previously (Figure 3A). Mitotic cells treated with barasertib had minimal phosphorylated AURKB. Phosphatase inhibition by okadaic acid increased AURKB phosphorylation levels, which was counteracted by pretreatment with barasertib. These effects are similar to those observed in *X. laevis* HSS and suggest that similar autophosphorylation regulates CPC kinase activity across organisms. Phosphatase inhibition also increased phosphorylation of two bands whose molecular weights suggested they are AURKA and AURKC. The sequence recognized by the antibody to phosphor-AUKRB is similar in these homologues. Only AURKB and AURKC phosphorylation was blocked by cotreatment of the AURKB inhibitor. This suggests that AURKC (not present in *X. laevis*) activity may also be dependent on AURKB activity or that AURKC may also be inhibited by barasertib, which has not been tested (Mortlock *et al.*, 2007). Phosphorylation levels of AURKA, on the other hand, were not affected by barasertib treatment. A band of similar molecular weight to AURKA did show barasertib-sensitive phosphorylation in *X. laevis* HSS (Figure 1D). It is possible that barasertib is less specific in *X. laevis*. Alternatively, cross-phosphorylation of AURKA and AURKB may occurs in HSS due to the lack of subcellular organization, or the upper band in HSS might in fact be a modified form of AURKB. No phosphorylated AURKB was observed in untreated HeLa cells (Supplemental Figure S5). In preliminary biochemical studies, we were unable to observe autophosphorylation of AURKB in response to phosphatase inhibition in HeLa cell lysates, potentially as a result of greater dilution in HeLa lysates than with *X. laevis* HSS. This prevented the use of sucrose gradients to measure hydrodynamic regulation of the CPC, and so instead we used FCS to obtain hydrodynamic information in live cells.

FCS measures the movement of fluorescent molecules in and out of a small illuminated volume and thus measures diffusion coefficients in live cells (Kim *et al.*, 2007). FCS requires a cell line in which the CPC is fluorescently tagged but with minimal artifacts resulting from overexpression of a single CPC subunit. Ideally, tagged cells should also have a high fluorescence signal per particle to maximize detection but a low concentration of tagged particles to facilitate measurement of intensity fluctuations. We tagged the C-terminus of the CDCA8 subunit in HeLa cells with a GFP-3xFLAG tag using a CRISPR/Cas9 strategy (Cong *et al.*, 2013) and sorted GFP-positive cells with FACS to obtain a cell line with stable expression. The concentration of tagged CDCA8 was too low to be detected in blots of whole-cell lysates; however, when the 3xFLAG tag was immunoprecipitated from both the tagged cell line and the parent line and blotted with an antibody against FLAG, only the tagged cell line exhibited a clear band at the expected molecular weight (62 kDa), without any other significant bands (Figure 3B). Similarly, immunoprecipitation of the FLAG tag or random immunoglobulin G (IgG) from whole-cell lysates of the tagged cell line followed by an anti-FLAG blot showed a protein band at 62 kDa only in the FLAG IP, indicating that the tagging was successful (Figure 3C). We also obtained HeLa cell lines expressing GFP-tagged INCENP and CDCA8 from bacterial artificial chromosome (BAC) constructs as a generous gift from Tony Hyman (MPI Dresden, Germany; Poser *et al.*, 2008). These express the tagged subunit from its endogenous promoter, but this expression occurs in addition to endogenous gene expression. Cell populations from each of the three cell types were fixed with paraformaldehyde and imaged by confocal microscopy (Figure 3D). All three lines showed the expected localization of the tagged CPC subunit to centromeres during metaphase and to midzone microtubules during anaphase/cytokinesis. The new CDCA8-GFP-3xFLAG CRISPR cell line exhibited significantly less background fluorescence than the BAC cell lines and had no expression in interphase cells, suggesting that a larger fraction of the tagged subunit was successfully incorporated into the CPC. We therefore selected the CRISPR-tagged line for FCS experiments.

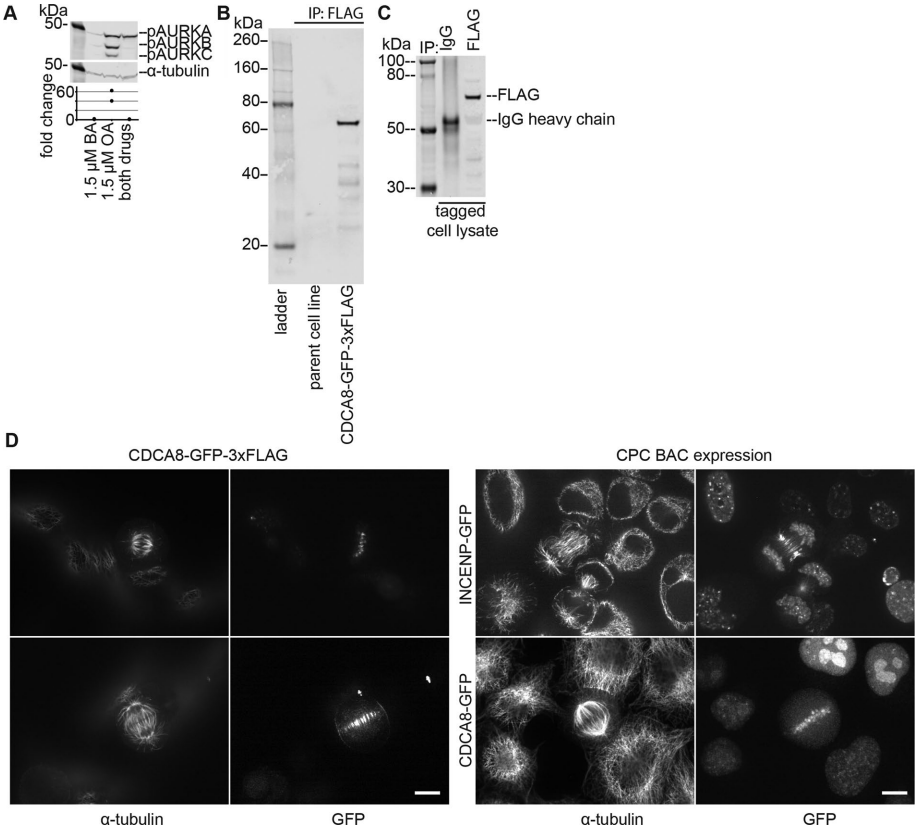

FIGURE 3: Tagging of CDCA8 in HeLa cells with GFP-3xFLAG. (A) HeLa cells were arrested in mitosis by overnight treatment with STLC and collected via mitotic shake-off, followed by washing with PBS. The indicated drugs were added to the final wash of the cells, after which the cells were lysed with freeze–thaw cycles. Cell lysates were then immunoblotted for pT232-AURK (recognizing pAURKA, pAURKB, and pAURKC) and α-tubulin. The *p* value between the barasertib- and okadaic acid–treated cells is 0.069; $n = 2$. (B) Lysates of the parent and tagged cell line were prepared as in A. Magnetic beads preloaded with an antibody against FLAG were used to immunoprecipitate (IP) tagged proteins from the lysates, and the resulting proteins were blotted for FLAG after separation via SDS–PAGE gel electrophoresis; $n = 2$. (C) Lysates of the tagged cell line were prepared as in A, and IPs were done with beads loaded with antibodies against random IgG or FLAG, followed by blotting for FLAG as in A; $n = 2$. (D) HeLa cells expressing GFP-tagged CPC were fixed with 4% paraformaldehyde, stained with an antibody against tubulin, and imaged with a spinning-disk confocal microscope at 60× magnification. Scale bars, 10 μm. Cells were imaged on three separate occasions.

To measure the diffusion of GFP-tagged CDCA8 in live mitotic cells, we applied two-photon confocal FCS using previously described methods (Needleman *et al.*, 2009). Mitotic cells were identified in unsynchronized cells by morphology. Conventional two-photon confocal imaging before FCS revealed CPC localization to centromeres as in Figure 3D. We then focused the FCS beam away from chromatin and other static bodies that might affect the measurement. Owing to the rapid time scales probed, FCS provides information only on the soluble pool of CPC. Representative primary FCS data presented as autocorrelation curves are shown in Figure 4A (top). The red and blue lines are the best fit to either one-or two-component models over multiple autocorrelation measurements. A model with a single diffusing species did not fit the data, whereas a two-species model gave a good fit in all cases (Figure 4A). An example of low residuals with this fit is shown in Figure 4A (bottom, blue line). The two-component model assumes two distinct populations undergoing normal diffusion (Kim *et al.*, 2007) with four fitting parameters: the two diffusion coefficients of each population (D_{slow} and D_{fast}) and the amplitudes of the autocorrelation functions of each population (G_{slow} and G_{fast}). We found that adding nocodazole to prevent astral microtubules from moving into the FCS voxel strongly reduced noise in autocorrelation graphs, and so we added nocodazole to all subsequent experiments. Nocodazole did not appear to affect the hydrodynamics of the soluble pool of CPC. The diffusion coefficient of the fast-diffusing population was roughly three times lower than that of monomeric GFP (Kuhn *et al.*, 2011) and is therefore likely the monomeric GFP-tagged CDCA8 outside of the CPC. The slow population, therefore, is presumed to be the complete CPC. Given large uncertainties in size-dependent viscosity in live cells, we did not attempt to calculate a hydrodynamic radius of the large complex.

With a live-cell hydrodynamic assay in hand, we added AURKB kinase (barasertib) and phosphatase (okadaic acid) inhibitors to test the effect of autophosphorylation on diffusion rates of the CPC. There was no systematic effect of okadaic acid or both drugs combined on G_{slow}/G_{fast}, suggesting the drugs did not cause dissociation of the CPC into its subunits (Figure 4B). D_{fast} exhibited no systematic changes in response to drugs, suggesting that unincorporated CDCA8 does not undergo hydrodynamic changes alone in response to phosphorylation (Figure 4C, right). However, D_{slow}, presumably corresponding to the diffusion constant of the native CPC, exhibited a time-dependent increase in response to okadaic acid, indicating that the complex diffuses faster as it becomes phosphorylated (Figure 4C, left, green squares). When barasertib was added in addition to okadaic acid, no increase in diffusion coefficient was observed, indicating the okadaic acid–induced change was due to autophosphorylation and requires AURKB activity (Figure 4C, left, red triangles).

We believe that the okadaic acid–induced, barasertib-inhibited increase in CPC diffusion rate measured by FCS is due to the same biochemistry as the okadaic acid–induced, barasertib inhibited decrease of the sedimentation coefficient of the CPC. An increase in diffusion coefficient upon phosphorylation is not consistent with an increased frictional coefficient of the complex and instead implies a shift to a lower molecular weight. Autophosphorylation could cause the CPC to shift to a lower molecular weight for two reasons: when inactive, the CPC could either be oligomerized or be bound to some large, unknown factor. The FCS data allow us to distinguish between these possibilities. G_{slow}/G_{fast} is equivalent to the ratio of fluorescent particles in each population multiplied by the ratio of the brightness of each population squared. If dephosphorylated CPC is an oligomer, then, in that state, one oligomer would contain multiple units of CDCA8-GFP but would only contribute one count to G_{slow}. On dissociation due to autophosphorylation, the apparent number of particles in the slow fraction would increase because each CPC containing one CDCA8-GFP subunit would be counted. The brightness of each particle in the slow fraction would decrease

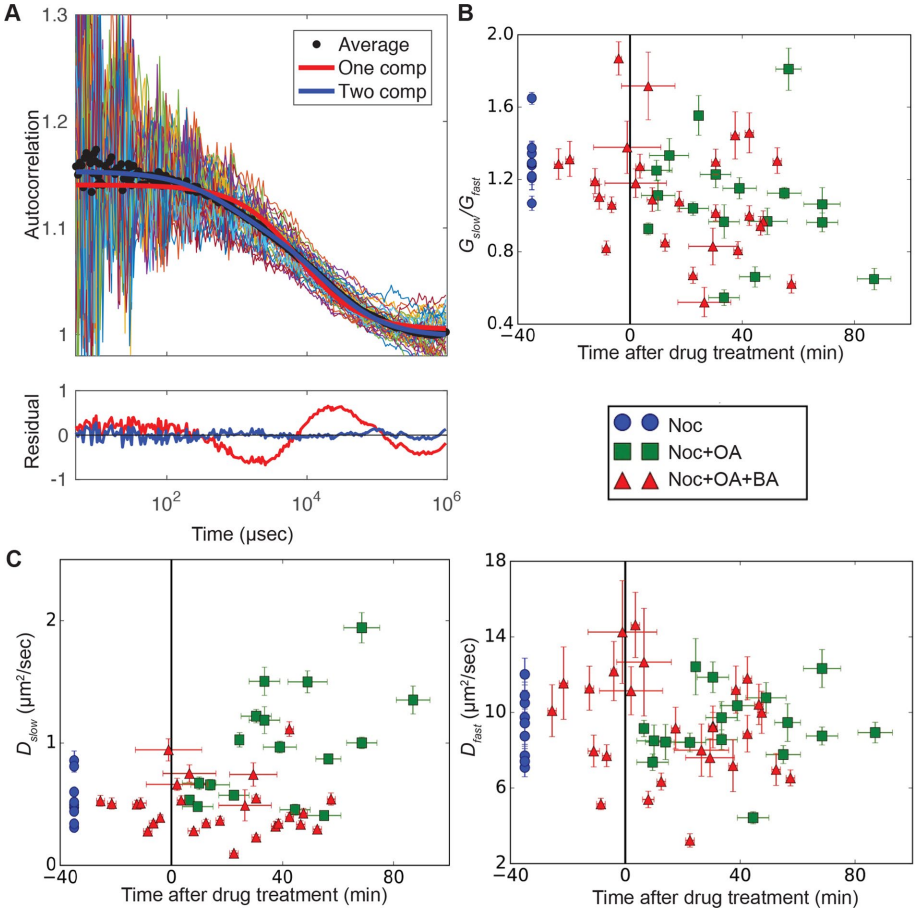

FIGURE 4: Fluorescence correlation spectroscopy of HeLa CDCA8-GFP-3xFLAG cells. Mitotic cells were identified and CPC localization to centrosomes confirmed by conventional imaging. The FCS measurement beam was directed into the cytoplasm near the edge of cells away from chromosomes to report on soluble CPC diffusion. (A) Example autocorrelation curves (top; black circles represent averages, and red and blue lines represent the fitted one- and two-component FCS models, respectively) and weighted residuals (bottom). (B) Ratio of amplitudes of slow- to fast-diffusing populations over time after drug treatment. Amplitudes are proportional to the number of molecules in a focal volume and molecular brightness squared. (C) Diffusion coefficients over time after drug treatment of the slow (left) and fast (right) populations in the presence of 1 μM nocodazole, with no further drug treatment (blue circles), or after treatment with only 250 nM okadaic acid (OA; green squares) or with both 250 nM OA and 250 nM barasertib (BA; red triangles). Each data point represents one mitotic cell, identified by observing round cell morphology and chromosomes in phase contrast, and averages were obtained by taking multiple measurements in each cell at each time point. Error bars represent the SD of the fitted parameters of the nonlinear regression.

by the same ratio. Therefore, when cells are treated with okadaic acid, G_{slow} would decrease, and G_{slow}/G_{fast} would decrease correspondingly. However, G_{slow}/G_{fast} did not change, regardless of drug treatment (Figure 4B). This suggests an absence of phosphoregulated oligomerization. Therefore the observed changes in hydrodynamic properties of the CPC are more likely due to its binding to some other large factor(s) when inactive, and this complex dissociates upon autophosphorylation.

Inactive CPC interacts with nucleoplasmin/nucleophosmin oligomers

To identify candidate inactive CPC-binding proteins, we returned to *X. laevis*, using an immunoprecipitation–mass spectrometry (IP-MS) strategy in both HSS and crude extract. Mitotic HSS was treated with barasertib, okadaic acid, or both drugs as in Figure 1B. We then immunoprecipitated INCENP and CDCA9 and subjected the samples to quantitative mass spectrometry analysis. We used tandem mass tags (TMT) after proteolysis to differentially label samples. Samples were pooled and analyzed using multinotch MS3 methods to quantify the amount of each peptide that came from each sample (Wuhr *et al.*, 2014). We ranked proteins by their enrichment in immunoprecipitates (IPs) with AURKB inhibition over AURKB activation (Supplemental Table S1). Attractive candidates had to meet two additional criteria: first, that they are abundant enough in frog eggs to bind all the CPC molecules, and second, that they have a large native molecular weight, sufficient to affect CPC hydrodynamic properties through binding. When these criteria were applied, the nucleoplasmin/nucleophosmin family of proteins (NPM) gave clear hits (Figure 5A). Similar results were seen in IP-MS experiments done in crude extract, for which we compared IPs without drug, where complex activation is induced by clustering on beads, and in the presence of ZM447439, an AURKB inhibitor (Supplemental Table S2). In addition to being highly enriched in IPs of CPC under inactive versus activating conditions, NPM family members are known to assemble into large homo- and hetero-pentameric and -decameric complexes, which function as molecular chaperones (Namboodiri *et al.*, 2004; Platonova *et al.*, 2011). They are also abundant in frog eggs. We observed peptides from both NPM2 and nucleoplasmin 3 in IP-MS experiments but not from the somatic isoform NPM1, which is not expressed in eggs. NPM2 is an embryonic isoform that is highly abundant in *X. laevis* eggs (~2000 nM), more than enough to sequester all of the CPC in the egg (~100 nM; Wuhr *et al.*, 2014). NPM3, which is much less abundant in eggs than NPM2 (~150 nM), likely hetero-oligomerizes with NPM2, and so it is not clear whether it interacts independently with the CPC. Other proteins that were identified as potential CPC inactive-state binding partners through IP-MS include partitioning defective 3 homologue (PARD3), a protein involved in asymmetrical cell division, and the chromatin protein chromobox protein homologue 3. These were less reproducible interactions than with NPMs 2 and 3 than in previous experiments in crude extract (Supplemental Table S2), the proteins are less abundant in eggs, and their native molecular weight is uncharacterized. We therefore focused on NPMs.

We next used IP-immunoblots from mitotic HSS to retest the IP-MS findings. Immunoprecipitations of random IgG, INCENP, CDCA9, and NPM2 from HSS dosed with no drug, barasertib, okadaic acid, or barasertib followed by okadaic acid were blotted with antibodies against INCENP and NPM2. We observed very strong interaction between both CPC components and NPM2 under AURKB-inhibited conditions but no interaction when phosphatases

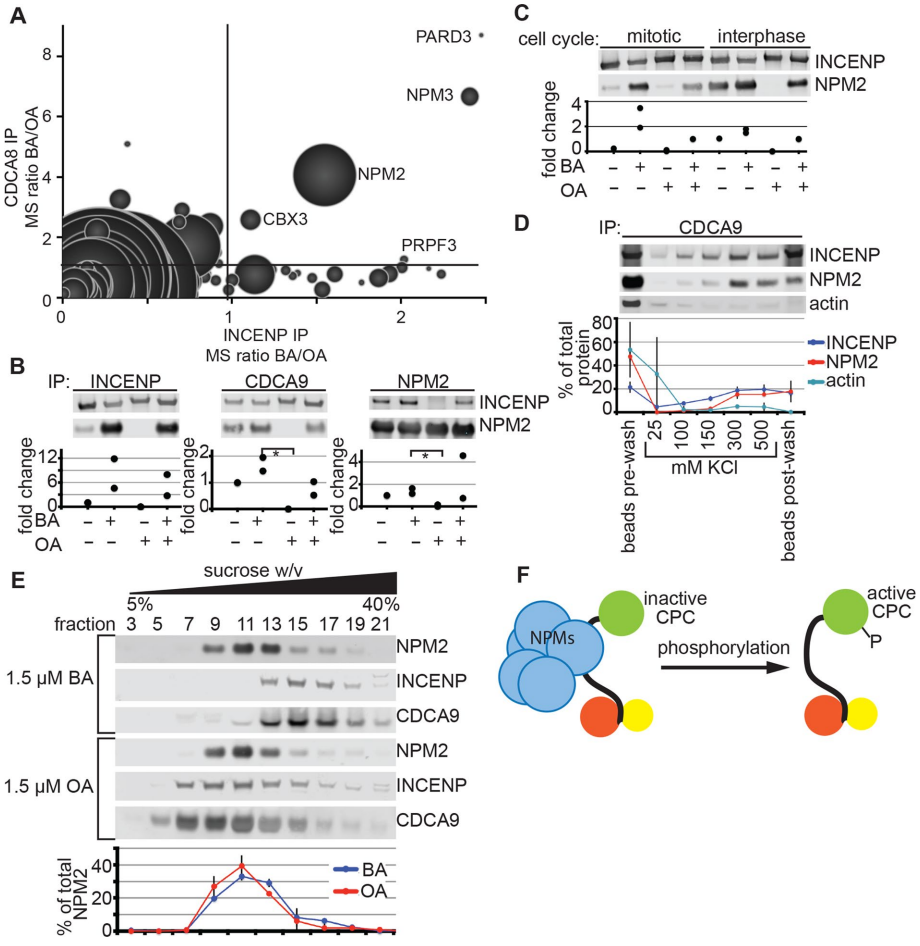

FIGURE 5: NPM2 interacts with inactive CPC. (A) CPC proteins were immunoprecipitated from mitotic HSS and analyzed via quantitative mass spectrometry. Protein counts were normalized to IgG IPs and the target protein (INCENP or CDCA9). Ratios for each protein were generated by dividing reporter ion counts from barasertib-treated samples by counts from okadaic acid–treated samples. Proteins with a ratio >1 (gridlines on plot) indicate enrichment in barasertib-treated samples over okadaic acid–treated samples. Labeled proteins are those with ratios >1 in both CDCA8 and INCENP IPs. Size of bubbles is proportional to the measured amount of protein in *X. laevis* extract (Wuhr *et al.*, 2014). Full lists of proteins and ratios are given in Supplemental Table S1. (B) Mitotic HSS was incubated with barasertib (BA), okadaic acid (OA), both, or neither as in Figure 1. Beads loaded with antibodies against *X. laevis* INCENP, CDCA9, and NPM2 were used for immunoprecipitations from treated mitotic HSS, and then the proteins on the beads were blotted with antibodies against INCENP and NPM2. Blots were quantified by dividing levels of the blotted protein by levels of the IP target protein. Fold change represents change in NPM2 levels (INCENP and CDCA9 IPs) or INCENP levels (NPM2 IP) after intensities were normalized by setting the DMSO lane to 1. Values of 0 indicate no detectable intensity. The *p* values between the BA and OA samples indicated by the asterisk are 0.029 (CDCA9 IP) and 0.043 (NPM2 IP); $n = 2$. Full blots, including molecular weight markers, are given in Supplemental Figure S6. (C) Crude *X. laevis* extract was cycled into interphase with the addition of calcium, and both mitotic and interphase extract were treated with drugs as in B. Beads loaded with antibody against CDCA9 were used for immunoprecipitation and immunoblotted for INCENP and NPM2. NPM2 blots were quantified as described, normalized to INCENP, and with the lane treated with both drugs set to 1. Full blot including molecular weight markers is given in Supplemental Figure S7. (D) The CPC was immunoprecipitated from mitotic HSS using the antibody raised against CDCA9. After four quick low-salt washes, beads were incubated in solutions of increasing salt for 5 min each. The proteins bound to the beads before and after the salt washes, as well as those in the entire volume of each salt wash, were separated via SDS–PAGE and protein levels analyzed by immunoblots of INCENP, NPM2, and actin. Protein levels were quantified as a percentage of the total of that protein. Error bars represent the SD; $n = 2$. Full blots including molecular weight markers are given in Supplemental Figure S8. (E) Sucrose gradients of barasertib (BA)- or okadaic acid (OA)–treated mitotic HSS were run as in Figure 1, except that fractions were one-third smaller. Every other fraction was immunoblotted for NPM2, INCENP, or CDCA9. NPM2 blots had 7.5 times less total protein concentration in each lane. NPM2 blots were quantified as in Figure 1. Error bars represent SD; $n = 2$. Full blots including molecular weight markers are given in Supplemental Figure S9. (F) Proposed model for phosphorylation-induced CPC hydrodynamic changes (CPC proteins: AURKB green, INCENP black line, CDCA8/9 orange, BIRC5 yellow). Pentameric or decameric NPM oligomers (blue) interact with the CPC when the CPC is inactive and unphosphorylated. This interaction may involve direct binding or be mediated by other proteins. When phosphatases are inhibited, NPMs dissociate and the CPC is activated.

were inhibited and AURKB is active (Figure 5B). The only exception was the immunoprecipitation of INCENP without any drugs. In this case, low levels of NPM2 were observed (much lower than in the barasertib-inhibited cases). We suspect that this is because the well-known AURKB-activating properties of the antibody raised against INCENP cause this sample to behave more like the okadaic acid–treated sample (Kelly *et al.*, 2007). We repeated the IP-immunoblot experiments in crude extract, which is arrested in mitosis, and extract induced to enter interphase by addition of calcium. As in HSS, NPM2 was strongly present in IPs of the CPC when the complex was inactive (barasertib treatment) but not when it was active (no treatment or treated with okadaic acid; Figure 5C). This result was similar in mitotic and interphase crude extract (Figure 5C).

To test the strength of the interaction between the CPC and NPM2, we immunoprecipitated the CPC using the antibody against CDCA9. We then subjected the beads to increasing concentrations of salt for brief periods and analyzed the amount of NPM2 dislodged from the beads (Figure 5D). We found that although substantial amounts of NPM2 were removed in the initial wash and lowest salt concentration, a population of NPM2 remained attached to the beads even at high salt concentrations. In fact, NPM2 was only completely removed from the beads at concentrations when the CPC itself starts to dissociate, as identified by the presence of INCENP in the washes at 300 and 500 mM KCl. This was not the case with another highly abundant protein, actin, which is not known to interact directly with the CPC. Actin was effectively removed by the initial low-salt washes, and very little remained at higher salt concentrations. This experiment suggests a fairly tight interaction between NPM2 and the CPC, although

we cannot formally distinguish direct binding from binding via additional proteins.

To test possible relevance of NPM2 complexes in the phosphoregulated sedimentation behavior of the CPC observed in Figures 1 and 2, we performed sucrose gradient analysis of *X. laevis* mitotic HSS treated with barasertib or okadaic acid and blotted for CPC and NPM2 subunits (Figure 5E). The major NPM2 peak sedimented at approximately 8S as previously reported, reflecting its pentameric or decameric structure (Laskey *et al.*, 1978). The fastest-sedimenting tail of the NPM2 peak cosedimented with inactive, fast-sedimenting CPC in barasertib-treated HSS, consistent with a model in which inactive CPC is complexed to NPM2 oligomers. In okadaic acid–treated HSS, both CPC subunits shifted to a slower-sedimenting peak as before, but the NPM2 sedimentation profile was largely unchanged, although NPM2 in the okadaic acid–treated sample seems to have a slightly lower sedimentation coefficient. Free NPM2 should have a lower sedimentation coefficient than NPM2 complexed with the CPC. However, NPM2 is approximately 20 times more abundant in the egg than CPC proteins, and the expected sedimentation change of NPM2 complexed with the CPC could be largely masked by the ~95% of NPM2 that does not interact with the CPC. We also examined the sedimentation pattern of histone H2A, because NPM2 is a known histone chaperone, but saw no apparent change between different drug treatments (Supplemental Figure S9)

Although not the focus of our analysis, our IP-MS data also revealed candidate proteins that interact more with active than with inactive CPC (Supplemental Table 1, with ratios in Figure 5A of <1). These included Kif20A, a kinesin that is believed to transport CPC toward microtubule plus ends during cytokinesis (Nguyen *et al.*, 2014). Further experimentation is required to evaluate the significance of these proteins.

DISCUSSION

We used a combination of nonspecific phosphatase inhibitor and specific kinase inhibitors to confirm previous studies showing that the CPC can be activated by autophosphorylation, most likely in-*trans* (Yasui *et al.*, 2004; Kelly *et al.*, 2007). We then investigated the effect of autophosphorylation on hydrodynamic behavior of the CPC in HSS from *X. laevis* eggs and live HeLa cells. We confirmed that the CPC can undergo a regulated change in hydrodynamic behavior, using sucrose gradient sedimentation (Figure 1). By comparing CPC sedimentation in mitotic and interphase HSS prepared without the use of phosphatase inhibitors (Figure 2), we showed that the decrease in S-value was triggered by autophosphorylation and not by cell cycle regulation as previously proposed (Bolton *et al.*, 2002). Using FCS to measure the diffusion of CPC in live HeLa cells, we found that autophosphorylation caused an increase in diffusion constant (Figure 4C). Combining the decrease in S-value observed by sucrose gradient sedimentation and the increase in diffusion coefficient observed by FCS upon treatment with a phosphatase inhibitor, we concluded that autophosphorylation caused a decrease in native molecular weight. This change was not due to reversal of an oligomeric state, because we observed no increase in the concentration of low–molecular weight CPC relative to unincorporated CDCA8 by FCS when the CPC was autophosphorylated (Figure 4B). The most likely explanation of these data is that inactive CPC is in complex with some large but diffusible particle, and autophosphorylation promotes disassembly of this complex**.** By IP-MS in egg extract, we identified a strong candidate for the CPC binding partner: the abundant oligomeric histone chaperone nucleophosmin (NPM2; Figure 5A). By reciprocal IP-Western blot, we confirmed that inactive CPC associates with NPM2 in egg extracts, regardless of cell cycle state, in both crude extracts and high-speed supernatants, and that this association is lost when the CPC autophosphophorylates in all cases (Figure 5, B and C). We attempted to perform similar experiments in HeLa cell lysates probing for NPM1, the somatic orthologue of NPM2. Our results were inconclusive, possibly due to the higher dilution in HeLa lysates. However, we suspect that inactive CPC binds to NMP1 in cells to account for the increase in diffusion constant we observed after autophosphorylation (Figure 4). Summarizing, we propose that inactive CPC is chaperoned by NPM complexes (Figure 5F**)**.

Our model for stabilization of inactive CPC by a chaperone-like factor has precedent; other kinases complex with nonkinase proteins that stabilize the inactive state. For example, in the inactive form of Src kinase, the kinase domain complexes with SH2 and SH3 domains in the same polypeptide, which helps keep the kinase inactive (Shalloway and Taylor, 1997). In general, the biochemistry of the inactive state of kinases deserves more experimental attention.

NPM family members exist as either highly disordered monomers or assemble into pentameric and decameric oligomers (Scaloni *et al.*, 2009, 2010; Duan-Porter *et al.*, 2014; Mitrea *et al.*, 2014), with well-established chaperone activity; indeed, the term "molecular chaperone" was first coined in 1978 by Laskey to describe the histone chaperone activity of nucleoplasmin (Laskey *et al.*, 1978; Gadad *et al.*, 2011). The formation of oligomers, required for histone chaperoning, is enhanced during mitosis, possibly by phosphorylation by cyclin/cyclin-dependent kinase (CDK) complexes (Lin *et al.*, 2016). NPM1 protects a number of different proteins from aggregation during thermal denaturation (Szebeni and Olson, 1999), despite having amyloid-like assembly properties itself (Di Natale *et al.*, 2015; Russo *et al.*, 2017), and escorts ribosomal subunits and other proteins from the nucleus to the cytoplasm (Maggi *et al.*, 2008; Mitrea *et al.*, 2016), binds RNA (Sagawa *et al.*, 2011; Hisaoka *et al.*, 2014) and G-quadruplex DNA (Federici *et al.*, 2010; Gallo *et al.*, 2012; Banuelos *et al.*, 2013; Chiarella *et al.*, 2013; Arcovito *et al.*, 2014; Scognamiglio *et al.*, 2014), helps repair DNA damage (Koike *et al.*, 2010), and assists in activating key mitotic kinases at the centrosome (Reboutier *et al.*, 2012). NPM1 is also a phosphorylation target of AURKB, PLK1, and other kinases (So *et al.*, 2012; Shandilya *et al.*, 2014). Both NPM1 and NPM2 are highly posttranslationally modified (Haindl *et al.*, 2008; Neo *et al.*, 2015; Okuwaki, 2008; Wilczek *et al.*, 2011) and bind histones H2A and H2B (Gadad *et al.*, 2011; Fernandez-Rivero *et al.*, 2016; Okuwaki *et al.*, 2001). NPM2 is particularly abundant in *X. laevis* eggs and is believed to sequester H2A and H2B (Onikubo *et al.*, 2015), to catalyze their assembly into chromatin and assist in transcription repression before the midblastula transition through histone sequestration (Laskey *et al.*, 1978; Platonova *et al.*, 2011; Finn *et al.*, 2012; Bouleau *et al.*, 2014) and may be involved in the decondensation of sperm chromatin (Burns *et al.*, 2003; Inoue *et al.*, 2011; Okuwaki *et al.*, 2012).

We can imagine several reasons that inactive CPC might be chaperoned by NPM complexes. Most obviously, this may prevent inactive CPC from competing with active CPC for binding to AURKB targets such as chromatin and microtubules. It may also slow autoactivation of the CPC. The CPC functions in a highly dynamic system, where its inactive and active forms rapidly interconvert, leading to local gradients in substrate phosphorylation on a micrometer scale (Afonso *et al.*, 2014). NPM sequestration of the inactive state may assist in tuning this delicate balance. NPM interactions may also catalyze nucleus–cytoplasm trafficking of the CPC; during interphase, NPMs are substrates for nuclear import through the Ran-KPNB1 (importin) system (Quensel *et al.*, 2004) and interact with exportin, ultimately localizing to nucleoli (Bolli *et al.*, 2007).

Nucleus–cytoplasm shuttling of the CPC is probably important in prophase regulation of chromatin and the nuclear envelope, and there are hints that the CPC is involved in nuclear pore reformation late in cytokinesis (Afonso *et al.*, 2014) and that the CPC phosphorylates nuclear proteins during mitosis (Dhanasekaran *et al.*, 2016). NPM also reportedly has important roles in mitosis; disrupting the protein with (+)-avrainvillamide, a small molecule that binds NPM1, results in supernumerary chromosomes (Mukherjee *et al.*, 2015). This may be a result of disrupting its inhibition of the CPC, although direct action of this abundant protein in mitotic progression is also a plausible explanation.

We suspect that NPMs bind the CPC near the AURKB subunit near the C-terminus of INCENP, for a few reasons. To have inhibitory function on AURKB, it is much more likely to be bound at or near the kinase in the complex. Second, the antibody against INCENP was raised from a C-terminal peptide, and this antibody is known to turn on AURKB activity (Kelly *et al.*, 2007). It may do this by knocking off inhibitory NPMs. Genetic analysis of the function of the CPC-NPM interaction will be challenging because both are essential for cell growth (Cutts *et al.*, 1999; Burns *et al.*, 2003; Grisendi *et al.*, 2005). Progress will likely depend on precise mapping, followed by mutation, of regions involved in the interaction. Depletion of NPM2 might be feasible in egg extract, although its abundance and the high likelihood that depleting NPM2 would codeplete CPC present significant experimental challenges.

The exact nature of the CPC-NPM interaction remains to be understood. We did not observe histones enriched in IPs of inactive CPC by MS or by Western blot, suggesting that binding of CPC and H2A/H2B to NPM2 might be mutually exclusive, but this point requires further investigation. It is also whether NPM2 or a protein that mediates the NPM2-CPC interaction recognizes some structural characteristic of the CPC present only when AURKB is inactive or whether NPM2 actually holds it in an inactive state. We also do not know the full extent of phosphorylation of CPC subunits or NPM family members by AURKB. In particular, the phosphorylation state of NPM may guide oligomerization, known to be important in other NPM chaperone functions. Finally, it is possible that other proteins that coimmunoprecipitate with inactive CPC, such as PARD3, play a role in NPM-CPC interactions, either by mediating the interaction itself or by adding additional functionality. Understanding the mechanistic implications of the NPM-CPC relationship will provide additional insight into cell division as a whole and potentially establish new proteins as drug targets for modulating cell division. Finally, our work extends the idea of NPM complexes as chaperones to a new substrate, the CPC. It will be interesting to ask what other substrates are chaperoned by NPM members in vivo and whether chaperone activity plays a role in the function of NPM1 mutants as oncogenes in acute myeloid leukemia (Bolli *et al.*, 2007).

MATERIALS AND METHODS

General

Experiments were repeated with at least two biological replicates unless otherwise indicated.

Materials

All chemicals were purchased from Sigma-Aldrich unless otherwise noted.

Antibodies

Antibodies against *X. laevis* INCENP and CDCA8 were raised against C-terminal peptides as previously described (Kelly *et al.*, 2007; Ozlu *et al.*, 2010). The antibody against *X. laevis* NPM2 was a generous gift of David Shetcher (Albert Einstein College of Medicine). Antibodies were purchased from commercial sources for pThr232-AURKB (2914S; Cell Signaling), MPM2 (16-155; Millipore), BIRC5 (2808S; Cell Signaling), FLAG (2368P; Cell Signaling), α-tubulin (T6199; Sigma-Aldrich), actin (MAB1501R; Fisher), histone H2A.Z (2718; Cell Signaling), random rabbit IgG (011-000-003; Jackson ImmunoResearch), goat anti-mouse DyLight 680 conjugated (35518; Thermo), goat anti-rabbit DyLight 800 conjugated (35571; Thermo), and Alexa Fluor 568 goat anti-mouse (A-11004; Life Technologies).

Western blots

Protein solutions were diluted in sample buffer (5×: 200 mM Tris-HCl, pH 6.8, 20% glycerol, 25% β-mercaptoethanol, 100 mg/ml SDS, 0.5 mg/ml bromophenol blue [Fluka]) and heated at 85–90°C for 5 (pAURKB blots) or 10 min (all other blots). The solutions were then separated on 4–12% NuPAGE Bis-Tris gels (Life Technologies) in MES buffer (Life Technologies). After gel electrophoresis, proteins were transferred to a nitrocellulose membrane (0.2 µm; Bio-Rad) or polyvinylidene fluoride membrane (0.2 µm, histone blots only; Bio-Rad) via wet transfer in 25 mM Tris base, 30 mM glycine, and 20% methanol buffer at 100 V for 2 h or 35 mA for 12–16 h at 4°C. Membranes were stained with Ponceau S stain (0.5% [wt/vol] Ponceau S [Mallinckrodt], 1% acetic acid [JT Baker]) before cutting the membrane into strips for analysis with multiple antibodies (if necessary). Membranes were blocked with Odyssey Blocking Buffer (phosphate-buffered saline [PBS]; LI-COR) for 1 h at room temperature or overnight at 4°C. Membranes were incubated with primary and secondary antibodies for 1 h at room temperature. Primary antibodies were used at 1:1000 (commercial) or 1 µg/ml (produced in-lab), and secondary antibodies were used at 1:10,000. Between the primary and secondary antibodies and after the secondary antibody, membranes were washed briefly with TBST (50 mM Trizma base, pH 7.6, 155 mM NaCl, 1% Tween 20), followed by TBST and two rounds of TBS (50 mM Trizma base, pH 7.6, 155 mM NaCl) for 10 min each at room temperature. Membranes were imaged with an Odyssey Infrared Imager (LI-COR), adjusting intensity of illumination to just below the oversaturation point. Blots were quantified using the gel analysis tools in ImageJ and plotted using Microsoft Excel. The SDs were also calculated in Microsoft Excel. The *p* values were calculated using one-sided *t* tests in Excel and marked by asterisks on the figures.

Homology analysis

Sequences of *X. laevis* and human CPC subunits were obtained from the UniProt database and compared using the NCBI BLAST tool, reporting the percentage identical.

X. laevis crude extract and HSS preparation

Mitotic HSS was prepared as previously described (Groen *et al.*, 2011). Standard protocols for the use of female *X. laevis* to obtain eggs by hormonal injection were approved by the Harvard Medical Area Standing Committee on Animals. S-CSF-XB-phosphate buffer (10 mM 4-(2-hydroxyethyl)-1-piperazineethanesulfonic acid [HEPES], pH 7.7, 100 mM KCl, 5 mM ethylene glycol tetraacetic acid [EGTA], 1 mM $MgCl_2$, 1 mM ATP, 1 mM GTP, 1 mM dithiothreitol, 5 mM glucose-6-phosphate, 1 mM creatine phosphate) was used for any dilutions. Interphase HSS was prepared as mitotic HSS, with the addition of cycling crude extract into interphase with calcium (Field *et al.*, 2014) and adding 2 µg/ml cyclohexamide before the hard spin. HSS was aliquoted, frozen in liquid nitrogen, and stored at –80°C until use. All HSS used in this work was mitotic unless otherwise indicated. Crude extract was used immediately after preparation.

HeLa cell culture and lysate preparation

HeLa cells were cultured in DMEM (Corning), 10% fetal bovine serum (Life Technologies), and 1% 100× penicillin/streptomycin solution (Corning) at 37°C, 5% CO_2, and 85% relative humidity. Mitotic HeLa lysates were prepared by dosing cells at ~70–80% confluency for 16 h with 3 µM STLC and then isolating mitotic cells via vigorous shake-off. The mitotic cells were washed three times with cold PBS (Corning) supplemented with STLC. After the removal of the final wash, protease inhibitors (leupeptin, pepstatin A, and chymostatin, 10 µg each as a 10 mg/ml mixture of all three in dimethyl sulfoxide [DMSO]), cytochalasin D (10 µg from a 10 mg/ml solution in DMSO), and nocodazole (7.5 µg as a 25 mM solution in DMSO) were added to the pellet, which was subsequently frozen in liquid nitrogen and thawed at room temperature three times to lyse cells. The lysate was then spun at 20,000 × *g* for 30 min at 4°C and the supernatant immediately used in experiments. For cells treated with okadaic acid (1 µM; Enzo) or barasertib (1 µM; ApexBio), the drug was added to the final wash of the cells and also just before lysis after removal of the final PBS wash.

Sucrose gradients

For each gradient (5–40% [wt/wt] in S-CSF-XB-phosphate), five step gradients (5, 14, 23, 32, and 40% sucrose) of equal volume (950 µl) were gently layered, highest density on the bottom, by pipetting into ½ × 2 inch ultraclear centrifuge tubes (Beckman Coulter) and allowed to diffuse overnight at 4°C into a continuous gradient. A 50-µl amount of HSS was treated with DMSO, barasertib, okadaic acid, or a combination of drugs (barasertib followed by okadaic acid) for 25 min per drug at room temperature before being diluted in half with S-CSF-XB-phosphate and pipetted gently onto the sucrose gradient. The sucrose gradients were then spun in tandem at 237,000 × *g* for 6 h at 4°C in an SW55Ti rotor (Beckman Coulter). Gradients were fractionated from the top by pipetting 130 µl (Figure 5) or 400 µl (Figures 1 and 2), and fractions 2–8 of 12 total fractions (Figures 1 and 2) and every other fraction from 3 to 21 of 36 total fractions were blotted for INCENP, CDCA9, and NPM2. BSA (4S) and bovine γ-globulin (7S) standards were run on parallel gradients and their fractionation determined by SDS–PAGE gel electrophoresis of all fractions, followed by staining with Coomassie blue (45% methanol [BDH], 10% glacial acetic acid [JT Baker], 0.25 g of Coomassie blue [Fluka]) and destaining with an aqueous solution of 7.5% acetic acid and 20% methanol.

Tagging of CDCA8-GFP-3xFLAG in HeLa cells

Guide RNA to cut at the C-terminal endogenous locus of CDCA8 in HeLa cells was designed using the tools at crispr.mit.edu. The top five hits were selected, and oligos (CACCGAATGAGACACCAAAGTTGAC, CACCGAGACACCAAAGTTGACAGGA, CACCGCAACTTTGGTGTCTCATTTG, CACCGAACTTTGGTGTCTCATTTGT, and CACCGAAAGTCCATCCTGTCAACTT and reverse complements [IDT]) to generate guide RNAs were cloned into the pX330-U6-Chimeric_BB-CBh-hSpCas9 plasmid (Addgene) following the depositing lab's instructions at crispr.genome-engineering.org (Cong *et al.*, 2013). Successful cloning was confirmed by sequencing using a U6 sequencing primer (Genewiz). Donor DNA was generated via isothermal assembly (Gibson *et al.*, 2009) of two Geneblocks (IDT) and a modified pET21a(+) backbone (Novagen) with a 650–base pair homology arm on the N-terminal side of the insert and a 597–base pair homology arm on the C-terminal side of the insert. The backbone was cut using *Eco*RI and *Zra*I restriction enzymes (NEB) for 2 h at 37°C. The Geneblocks were amplified in PCRs using oligos with 30–base pair overlaps with the backbone and 20–base pair priming sequences in Phusion high-fidelity PCR master mix with HF buffer using the program 1) 94°C, 2 min, 2) 94°C, 30 s, 3) 54°C, 30 s, 4) 72°C, 2 min, 5) repeat steps 2–4 nine more times, 6) 94°C, 30 s, 7) 72°C, 2 min, 8) repeat steps 6 and 7 24 more times, and 9) 72°C, 10 min. Cut backbone and PCR products were purified on 1% agarose (Lonza) gels in TAE buffer (40 mM Tris base, 1 mM EDTA, 5.7% acetic acid), followed by DNA isolation using the QIAquick Gel Extraction kit (Qiagen) according to the manufacturer's instructions. Backbone (3 µl) and inserts (1 µl each) were combined and annealed together at 50°C for 30 min in 15-µl isothermal assembly buffer (Gibson *et al.*, 2009). The reaction was then transformed into 5-alpha competent *Escherichia coli* (high efficiency; NEB) according to the manufacturer's instructions. Cloning was confirmed by sequencing using a T7 reverse primer (Genewiz). HeLa cells (24×10^4 per well of a six-well plate [Corning]) were transfected simultaneously with the two plasmids using Lipofectamine 3000 (Life Technologies) according to the manufacturer's instructions (2 µg of donor DNA, 1 µg of guide/Cas9 pX330 DNA, 3.75 µg of Lipofectamine 3000, and 6 µl of P3000). Cells were then selected by FACS using a BD FACSAria IIu-3 Laser with a 488-nm laser. All guides produced fluorescent cells with proper localization of GFP to the midzone in mitosis (see *Confocal microscopy*). The population with the most cells after FACS sorting from the first guide sequence listed was used for subsequent experiments.

Confocal microscopy

Cells were grown on glass coverslips (22 × 22 mm, no. 1.5; VWR), fixed with 4% paraformaldehyde in PBS (Corning) for 15 min at room temperature, permeabilized with 0.2% Triton X-100 in PBS (PBST) for 20 min at room temperature, and immunostained with antibodies against α-tubulin (1:400 in PBST, 1 h, room temperature) and Alexa Fluor 568 goat anti-mouse (1:400 in PBST, 1 h, room temperature), followed by three 5-min washes in PBST. The coverslips were then placed onto 10-µl droplets of 10% glycerol in PBST on clean coverslips and sealed with Valap (1:1:1 lanolin, paraffin [Fluka], and petroleum jelly). Images were obtained at the Nikon Imaging Center at Harvard Medical School at room temperature using a 60× oil Plan Apo 1.49 numerical aperture (NA) objective lens (Nikon) on a confocal Nikon Ti motorized inverted microscope equipped with a Yokogawa CSU-X1 spinning disk (Spectral Applied Research Aurora Borealis modification), Perfect Focus, a Prior Proscan II motorized stage, a Spectral Applied Research LMM-5 laser merge module (excitation:emission 488:480/40, 561:620/60, 642:700/75) with acousto-optical tunable filter–controlled solid-state lasers, and a Hamamatsu ORCA-AG cooled charge-coupled device camera, driven by MetaMorph. Images were prepared for publication using ImageJ. No modifications were made to images beyond minor brightness and contrast adjustments and cropping to center images on mitotic cells.

Fluorescence correlation spectroscopy

FCS measurements were performed on a Nikon Eclipse Ti microscope using two-photon excitation from a Ti:Sapphire pulsed laser (Mai-Tai; Spectral-Physics) with 80-MHz repetition rate and ~70-fs pulse width at 920-nm wavelength. The excitation light was expanded and collimated to fully utilize the numerical aperture of the water immersion objective (CFI Apo 40 × WI, NA 1.25; Nikon) that focuses the light into the sample. The intensity of excitation light was modulated to 3 mW at the objective by a combination of half-wave plate and polarizing beam splitter (Thorlab). Cells were grown to 80–90% confluency on glass coverslips with #1.5 thickness, 25 mm diameter, and poly-D-lysine coating (Neuvitro). During imaging, we

used a home-built temperature-controlled chamber to maintain cells at 37°C in an imaging medium, FluoroBrite DMEM (Life Technologies) supplemented with 10 mM HEPES and 2 mM L-glutamine, covered with mineral oil. A hybrid detector (HPM-100-40; Becker & Hickl) with 510/42 bandpass filter (Chroma) and TCSPC module (SPC-150; Becker & Hickl) were used to collect GFP fluorescence and calculate the normalized autocorrelation function of the fluorescence intensity fluctuations.

Contraction assays

X. laevis crude mitotic and interphase extract were prepared as described. Droplets of extract (1 µl) were carefully placed in a plastic Petri dish containing mineral oil (Field *et al.*, 2011). Drops were side-illuminated with light (LED Spotlight; AmScope) and imaged with a dissecting scope (Leica MZFLIII) fitted with a PLANAPO 1.0× objective and an 18.0 monochrome without infrared camera (Diagnostic Instruments) and MetaMorph. Images were processed using ImageJ.

FCS data analysis

Each autocorrelation function was collected for 10 s while the excitation beam was parked close to the edge of a mitotic cell. From 20 to 50 autocorrelation functions were averaged after the outliers were removed. The following two-component FCS model was fitted to the average autocorrelation function:

$$G_D(\tau) = \sum_{i=\text{slow, fast}} G_i \left(\frac{1}{1+\tau/\tau_{D,i}} \right) \left(\frac{1}{1+S^2\left(\tau/\tau_{D,i}\right)} \right)^{\frac{1}{2}} + G_\infty$$

where G_i and $\tau_{D,i}$ are the amplitude and diffusion time of each component, respectively, and S is the ratio between the equatorial (w_{xy}) and axial (w_z) radii of the focal volume. Before every FCS experiment, w_{xy} and w_z were determined from the FCS measurements on calibration samples, 9.7 and 97 nM Alexa 488 dye in water, assuming that the diffusion coefficient of Alexa 488 is 435 µm^2/s (Petrasek and Schwille, 2008). The nonlinear fitting was performed by a MATLAB built-in function, *nlinfit*, with the observation weight specified to the inverse of the SD of the autocorrelation functions. The diffusion time, $\tau_{D,i}$, was converted into the diffusion coefficient, D_i, using the relationship

$$D_i = \frac{w_{xy}^2}{8\tau_{D,i}}, \quad i = \text{slow, fast}$$

Immunoprecipitation

Anti-FLAG M2 beads or Dynabeads Protein A beads (Life Technologies), charged with INCENP, CDCA9, NPM1, and NPM2 antibody at saturating levels according to the manufacturer's instructions, were incubated end over end with lysate, crude *X. laevis* egg extract, or HSS after drug treatment for at least 45 min at 4°C. Beads were separated from the lysate on a DynaMag-2 Magnet (Life Technologies) and washed with cold 10 mM HEPES, 1 mM $MgCl_2$, 25 mM KCl, 1 mM EGTA, and 0.01% Tween 20, pH 7.7, at least four times and subjected to immunoblot analysis or quantitative mass spectrometry (Tween 20 omitted for mass spectrometry experiments). For immunoprecipitations from crude extract, cytochalasin D was omitted from the extract preparation (Field *et al.*, 2014) to permit contraction assays (described later). Cytochalasin D was then added to the extract along with other drugs for the immunoprecipitation.

Quantitative MS

Immunoprecipitations were performed as described. The beads were taken up in 5 µl of 8 M guanidine-HCl, incubated at 60°C for 20 min, and diluted to 2 M guanidine-HCl with 20 mM *N*-(2-hydroxyethyl)piperazine-*N*′-(4-butanesulfonic acid) (HEPBS), pH 9.0. A 0.4-µl amount of 2 mg/ml LysC (Wako Chemical) was added and incubated at room temperature for 14 h. The slurry was then diluted again to 0.5 M guanidine-HCl with the same HEPBS solution, and an additional 0.4 µl of 2 mg/ml LysC was added along with 0.8 µl or 0.5 mg/ml trypsin (Promega sequencing grade), and the solution was incubated at 37°C for 8 h. After transfer to a fresh tube, the supernatant was removed by vacuum overnight. The pellets were diluted in 20 µl of 300 mM HEPES, pH 8.0, and 3 µl of TMT (Thermo). Dry acetonitrile at 5 mg/250 µl was added to the solution, which was then incubated at room temperature for 2 h. A 3-µl amount of 5% hydroxylamine (99.999% pure; Sigma-Aldrich) was added, followed by a 15-min room temperature incubation, after which the solvent was removed by vacuum overnight. The solution was acidified to pH ~1 with phosphoric acid, and a C18 stage-tip was done to desalt the sample (Rappsilber *et al.*, 2007). All solvent was removed, and the sample was resuspended in 6 µl of 1% formic acid. A 3-µl amount of the sample was shot on an Orbitrap Lumos instrument as previously reported (Wuhr *et al.*, 2015). Samples were normalized by IgG IPs and by the amount of target protein (INCENP or CDCA8). The normalized amount of protein in the barasertib-treated sample was divided by that in the okadaic acid–treated sample, and hits were considered to be those proteins that had values >1.

Salt elution assay

The antibody against CDCA9 was used to immunoprecipitate the CPC from 100 µl of mitotic HSS as described and washed with the same buffer as before briefly four times. Half of the beads were isolated. The other half was subjected to five washes of 15-µl wash buffers for 5 min on ice per wash. The salt concentration was increased from 25 mM KCl to 100, 150, 300, and finally 500 mM KCl, removing each wash before adding the next one. A 5-µl amount of sample buffer was added to each wash. Bead aliquots from both before and after the washes were resuspended in 15 µl of sample buffer. The beads and washes were analyzed by SDS–PAGE, followed by immunoblotting as described.

ACKNOWLEDGMENTS

We gratefully thank D. Shechter (Albert Einstein College of Medicine) for the gift of NPM2 antibody, T. Hyman (MPI Dresden) for BAC cell lines, and S. Gygi (HMS Cell Biology) for mass spectrometry resources. We thank the Nikon Imaging Center at Harvard Medical School for confocal microscopy resources and assistance. We also thank C. Field for critical reading of the manuscript, J. Pelletier for assistance in *X. laevis* extract preparation, and E. Boke and J.-H. Wang for helpful discussions. This work was supported by National Institutes of Health Grant NIH-GM39565. The FCS work (T.Y.Y. and D.J.N.) was supported by National Science Foundation Grants DBI-0959721 and DMR-0820484. M.S. was supported by Ruth L Kirschstein National Institutes of Health F31 Predoctoral Fellowship 5F31GM116451. The content is solely the responsibility of the authors and does not necessarily represent the official views of the National Institutes of Health.

REFERENCES

Adams RR, Wheatleya SP, Gouldsworthy AM, Kandels-Lewis SE, Carmena M, Smythe C, Gerloff DL, Earnshaw WC (2000). INCENP binds the Aurora-related kinase AIRK2 and is required to target it to chromosomes, the central spindle and cleavage furrow. Curr Biol 10, 1075–1078.

Afonso O, Matos I, Pereira AJ, Aguiar P, Lampson MA, Maiato H (2014). Feedback control of chromosome separation by a midzone Aurora B gradient. Science 345, 332–336.

Arcovito A, Chiarella S, Della Longa S, Di Matteo A, Lo Sterzo C, Scaglione GL, Federici L (2014). Synergic role of nucleophosmin three-helix bundle and a flanking unstructured tail in the interaction with G-quadruplex DNA. J Biol Chem 289, 21230–21241.

Banuelos S, Lectez B, Taneva SG, Ormaza G, Alonso-Marino M, Calle X, Urbaneja MA (2013). Recognition of intermolecular G-quadruplexes by full length nucleophosmin. Effect of a leukaemia-associated mutation. FEBS Lett 587, 2254–2259.

Berrabah W, Aumercier P, Lefebvre P, Staels B (2011). Control of nuclear receptor activities in metabolism by post-translational modifications. FEBS Lett 585, 1640–1650.

Bishop JD, Schumacher JM (2002). Phosphorylation of the carboxyl terminus of inner centromere protein (INCENP) by the Aurora B kinase stimulates Aurora B kinase activity. J Biol Chem 277, 27577–27580.

Bolli N, Nicoletti I, De Marco MF, Bigerna B, Pucciarini A, Mannucci R, Martelli MP, Liso A, Mecucci C, Fabbiano F, *et al.* (2007). Born to be exported: COOH-terminal nuclear export signals of different strength ensure cytoplasmic accumulation of nucleophosmin leukemic mutants. Cancer Res 67, 6230–6237.

Bolton MA, Lan W, Powers SE, McCleland ML, Kuang J, Stukenberg PT (2002). Aurora B kinase exists in a complex with survivin and INCENP and its kinase activity is stimulated by survivin binding and phosphorylation. Mol Biol Cell 13, 3064–3077.

Bouleau A, Desvignes T, Traverso JM, Nguyen T, Chesnel F, Pauvel C, Bobe J (2014). Maternally inherited npm2 mRNA is crucial for egg developmental competence in zebrafish. Biol Reprod 91, 43, 1–9.

Burns KH, Viveiros MM, Ren Y, Wang P, DeMayo FJ, Frail DE, Eppig JJ, Matzuk MM (2003). Roles of NPM2 in chromatin and nucleolar organization in oocytes and embryos. Science 300, 633–636.

Carmena M, Wheelock M, Funabiki H, Earnshaw WC (2012). The chromosomal passenger complex (CPC): from easy rider to the godfather of mitosis. Nat Rev Mol Cell Biol 13, 789–803.

Chiarella S, De Cola A, Scaglione GL, Carletti E, Graziano V, Barcaroli D, Lo Sterzo C, Di Matteo A, Di Ilio C, Falini B, *et al.* (2013). Nucleophosmin mutations alter its nucleolar localization by impairing G-quadruplex binding at ribosomal DNA. Nucleic Acids Res 41, 3228–3239.

Cong L, Ran FA, Cox D, Lin S, Barretto R, Habib N, Hsu PD, Wu X, Jiang W, Marraffini LA, Zhang F (2013). Multiplex genome engineering using CRISPR/Cas systems. Science 339, 819–823.

Cooke CA, Heck MMS, Earnshaw WC (1987). The inner centromere protein (INCENP) antigens: movement from inner centromere to midbody during mitosis. J Cell Biol 105, 2053–2067.

Cutts SM, Fowler KJ, Kile BT, Hii LLP, O'Dowd RA, Hudson DF, Saffery R, Kalitsis P, Earle E, Choo KHA (1999). Defective chromosome segregation, microtubule bundling and nuclear bridging in inner centromere protein gene (Incenp)-disrupted mice. Hum Mol Genet 8, 1145–1155.

Dhanasekaran K, Kumari S, Boopathi R, Shima H, Swaminathan A, Bachu M, Ranga U, Igarashi K, Kundu TK (2016). Multifunctional human transcriptional coactivator protein PC4 is a substrate of Aurora kinases and activates the Aurora enzymes. FEBS J 283, 968–985.

Di Natale C, Scognamiglio PL, Cascella R, Cecchi C, Russo A, Leone M, Penco A, Relini A, Federici L, Di Matteo A, *et al.* (2015). Nucleophosmin contains amyloidogenic regions that are able to form toxic aggregates under physiological conditions. FASEB J 29, 3689–3701.

Duan-Porter WD, Woods VL Jr, Maurer KD, Li S, Rosen A (2014). Dynamic conformations of nucleophosmin (NPM1) at a key monomer-monomer interface affect oligomer stability and interactions with granzyme B. PLoS One 9, e115062.

Federici L, Arcovito A, Scaglione GL, Scaloni F, Lo Sterzo C, Di Matteo A, Falini B, Giardina B, Brunori M (2010). Nucleophosmin C-terminal leukemia-associated domain Interacts with G-rich quadruplex forming DNA. J Biol Chem 285, 37138–37149.

Fernandez-Rivero N, Franco A, Velazquez-Campoy A, Alonso E, Muga A, Prado A (2016). A quantitative characterization of nucleoplasmin/histone complexes reveals chaperone versatility. Sci Rep 6, 32114.

Field CM, Groen AC, Nguyen PA, Mitchison TJ (2015). Spindle-to-cortex communication in cleaving, polyspermic Xenopus eggs. Mol Biol Cell 26, 3628–3640.

Field CM, Nguyen PA, Ishihara K, Groen AC, Mitchison TJ (2014). Xenopus egg cytoplasm with intact actin. Methods Enzymol 540, 399–415.

Field CM, Wuhr M, Anderson GA, Kueh HY, Strickland D, Mitchison TJ (2011). Actin behavior in bulk cytoplasm is cell cycle regulated in early vertebrate embryos. J Cell Sci 124, 2086–2095.

Finn RM, Ellard K, Eirin-Lopez JM, Ausio J (2012). Vertebrate nucleoplasmin and NASP: egg histone storage proteins with multiple chaperone activities. FASEB J 26, 4788–4804.

Gadad SS, Senapati P, Syed SH, Rajan RE, Shandilya J, Swaminathan V, Chatterjee S, Colombo E, Dimitrov S, Pelicci PG, *et al.* (2011). The multifunctional protein nucleophosmin (NPM1) is a human linker histone H1 chaperone. Biochemistry 50, 2780–2789.

Gadea BB, Ruderman JV (2006). Aurora B is required for mitotic chromatin-induced phosphorylation of Op18/Stathmin. Proc Natl Acad Sci USA 103, 4493–4498.

Gallo A, Lo Sterzo C, Mori M, Di Matteo A, Bertini I, Banci L, Brunori M, Federici L (2012). Structure of nucleophosmin DNA-binding domain and analysis of its complex with a G-quadruplex sequence from the c-MYC promoter. J Biol Chem 287, 26539–26548.

Gassmann R, Carvalho A, Henzing AJ, Ruchaud S, Hudson DF, Honda R, Nigg EA, Gerloff DL, Earnshaw WC (2004). Borealin: a novel chromosomal passenger required for stability of the bipolar mitotic spindle. J Cell Biol 166, 179–191.

Gibson DG, Young L, Chuang R-Y, Venter JC, Hutchison CA, Smith HO (2009). Enzymatic assembly of DNA molecules up to several hundred kilobases. Nat Methods 6, 343–345.

Grisendi S, Bernardi R, Rossi M, Cheng K, Khandker L, Manova K, Pandolfi PP (2005). Role of nucleophosmin in embryonic development and tumorigenesis. Nature 437, 147–153.

Groen AC, Coughlin M, Mitchison TJ (2011). Microtubule assembly in meiotic extract requires glycogen. Mol Biol Cell 22, 3139–3151.

Haindl M, Harasim T, Eick D, Muller S (2008). The nucleolar SUMO-specific protease SENP3 reverses SUMO modification of nucleophosmin and is required for rRNA processing. EMBO Rep 9, 273–279.

Hisaoka M, Nagata K, Okuwaki M (2014). Intrinsically disordered regions of nucleophosmin/B23 regulate its RNA binding activity through their inter- and intra-molecular association. Nucleic Acids Res 42, 1180–1195.

Honda R, Koerner R, Nigg EA (2003). Exploring the functional interactions between Aurora B, INCENP, and survivin in mitosis. Mol Biol Cell 14, 3325–3341.

Hu C-K, Ozlu N, Coughlin M, Steen JJ, Mitchison TJ (2012). Plk1 negatively regulates PRC1 to prevent premature midzone formation before cytokinesis. Mol Biol Cell 23, 2702–2711.

Inoue A, Ogushi S, Saitou M, Suzuki MG, Aoki F (2011). Involvement of mouse nucleoplasmin 2 in the decondensation of sperm chromatin after fertilization. Biol Reprod 85, 70–77.

Jeyaprakash AA, Klein UR, Lindner D, Ebert J, Nigg EA, Conti E (2007). Structure of a survivin-borealin-INCENP core complex reveals how chromosomal passengers travel together. Cell 131, 271–285.

Kelly AE, Sampath SC, Maniar TA, Woo EM, Chait BT, Funabiki H (2007). Chromosomal enrichment and activation of the Aurora B pathway are coupled to spatially regulate spindle assembly. Dev Cell 12, 31–43.

Kim SA, Heinze KG, Schwille P (2007). Fluorescence correlation spectroscopy in living cells. Nat Methods 4, 963–973.

Koike A, Nishikawa H, Wu W, Okada Y, Venkitaraman AR, Ohta T (2010). Recruitment of phosphorylated NPM1 to sites of DNA damage through RNF8-dependent ubiquitin conjugates. Cancer Res 70, 6746–6756.

Koryakina Y, Ta HQ, Gioeli D (2014). Androgen receptor phosphorylation: biological context and functional consequences. Endocr Relat Cancer 21, T131–T145.

Kuang J, Ashorn CL, Gonzalez Kuyvenhoven M, Penkala JE (1994). Cdc25 is one of the MPM-2 antigens involved in the activation of maturation-promoting factor. Mol Biol Cell 5, 611.

Kuhn T, Ihalainen TO, Hyvaluoma J, Dross N, Willman SF, Langowski J, Vihinen-Ranta M, Timonen J (2011). Protein diffusion in mammalian cell cytoplasm. PLoS One 6, e22962.

Laskey RA, Honda BM, Mills AD, Finch JT (1978). Nucleosomes are assembled by an acidic protein which binds histones and transfers them to DNA. Nature 275, 416–420.

Lin J, Hisaoka M, Nagata K, Okuwaki M (2016). Functional characterization and efficient detection of Nucleophosmin/NPM1 oligomers. Biochem Biophys Res Commun 480, 702–708.

Mackay AM, Ainsztein AM, Eckley DM, Earnshaw WC (1998). A dominant mutant of inner centromere protein (INCENP), a chromosomal protein, disrupts prometaphase congression and cytokinesis. J Cell Biol 140, 991–1002.

Maggi LB Jr, Kuchenruether M, Dadey DYA, Schwope RM, Grisendi S, Townsend RR, Pandolfi PP, Weber JD (2008). Nucleophosmin serves as a rate-limiting nuclear export chaperone for the mammalian ribosome. Mol Cell Biol 28, 7050–7065.

Mitchison TJ, Nguyen P, Coughlin M, Groen AC (2013). Self-organization of stabilized microtubules by both spindle and midzone mechanisms in Xenopus egg cytosol. Mol Biol Cell 24, 1559–1573.

Mitrea DM, Cika JA, Ban D, Nourse A, Kriwacki RW, Cika JA, Guy CS, Banerjee PR, Deniz AA, Stanley CB, *et al.* (2016). Nucleophosmin integrates within the nucleolus via multi-modal interactions with proteins displaying R-rich linear motifs and rRNA. Elife 5, e13571.

Mitrea DM, Grace CR, Buljan M, Yun M-K, Pytel NJ, Satumba J, Nourse A, Park C-G, Babu MM, White SW, Kriwacki RW (2014). Structural polymorphism in the N-terminal oligomerization domain of NPM1. Proc Natl Acad Sci USA 111, 4466–4471.

Mortlock AA, Foote KM, Heron NM, Jung FH, Pasquet G, Lohmann J-JM, Warin N, Renaud F, De Savi C, Roberts NJ, *et al.* (2007). Discovery, synthesis, and in vivo activity of a new class of pyrazolylamino quinazolines as selective inhibitors of Aurora B kinase. J Med Chem 50, 2213–2224.

Mukherjee H, Chan K-P, Andresen V, Hanley ML, Gjertsen BT, Myers AG (2015). Interactions of the natural product (+)-avrainvillamide with nucleophosmin and exportin-1 mediate the cellular localization of nucleophosmin and its AML-associated mutants. ACS Chem Biol 10, 855–863.

Namboodiri VMH, Akey IV, Schmidt-Zachmann MS, Head JF, Akey CW (2004). The structure and function of Xenopus NO38-core, a histone chaperone in the nucleolus. Structure 12, 2149–2160.

Needleman DJ, Xu Y, Mitchison TJ (2009). Pin-hole array correlation imaging: highly parallel fluorescence correlation spectroscopy. Biophys J 96, 5050–5059.

Neo SH, Itahana Y, Alagu J, Kitagawa M, Guo AK, Lee SH, Tang K, Itahana K (2015). TRIM28 is an E3 ligase for ARF-mediated NPM1/B23 SUMOylation that represses centrosome amplification. Mol Cell Biol 35, 2851–2863.

Nguyen PA, Groen AC, Loose M, Ishihara K, Wuehr M, Field CM, Mitchison TJ (2014). Spatial organization of cytokinesis signaling reconstituted in a cell-free system. Science 346, 244–247.

Okuwaki M (2008). The structure and functions of NPM1/Nucleophosmin/B23, a multifunctional nucleolar acidic protein. J Biochem 143, 441–448.

Okuwaki M, Matsumoto K, Tsujimoto M, Nagata K (2001). Function of nucleophosmin/B23, a nucleolar acidic protein, as a histone chaperone. FEBS Lett 506, 272–276.

Okuwaki M, Sumi A, Hisaoka M, Saotome-Nakamura A, Akashi S, Nishimura Y, Nagata K (2012). Function of homo- and hetero-oligomers of human nucleoplasmin/nucleophosmin family proteins NPM1, NPM2 and NPM3 during sperm chromatin remodeling. Nucleic Acids Res 40, 4861–4878.

Onikubo T, Nicklay JJ, Xing L, Warren C, Anson B, Wang W-L, Burgos Ruff ES SE, Shabanowitz J, Cheng RH, *et al.* (2015). Developmentally regulated post-translational modification of nucleoplasmin controls histone sequestration and deposition. Cell Rep 10, 1735–1748.

Ozlu N, Monigatti F, Renard BY, Field CM, Steen H, Mitchison TJ, Steen JJ (2010). Binding partner switching on microtubules and Aurora-B in the mitosis to cytokinesis transition. Mol Cell Proteomics 9, 336–350.

Petrasek Z, Schwille P (2008). Precise measurement of diffusion coefficients using scanning fluorescence correlation spectroscopy. Biophys J 94, 1437–1448.

Platonova O, Akey IV, Head JF, Akey CW (2011). Crystal structure and function of human nucleoplasmin (Npm2): a histone chaperone in oocytes and embryos. Biochemistry 50, 8078–8089.

Portella G, Passaro C, Cheiffi P (2011). Aurora B: a new prognostic marker and therapeutic target in cancer. Curr Med Chem 18, 482–496.

Poser I, Sarov M, Hutchins JRA, Heriche J-K, Toyoda Y, Pozniakovsky A, Weigl D, Nitzsche A, Hegemann B, Bird AW, *et al.* (2008). BAC TransgeneOmics: a high-throughput method for exploration of protein function in mammals. Nat Methods 5, 409–415.

Quensel C, Friedrich B, Sommer T, Hartmann E, Kohler M (2004). In vivo analysis of importin α proteins reveals cellular proliferation inhibition and substrate specificity. Mol Cell Biol 24, 10246–10255.

Rappsilber J, Mann M, Ishihama Y (2007). Protocol for micro-purification, enrichment, pre-fractionation and storage of peptides for proteomics using StageTips. Nat Protoc 2, 1896–1906.

Reboutier D, Troadec M-B, Cremet J-Y, Fukasawa K, Prigent C (2012). Nucleophosmin/B23 activates Aurora A at the centrosome through phosphorylation of serine 89. J Cell Biol 197, 19–26.

Russo A, Diaferia C, La Manna S, Giannini C, Sibillano T, Accardo A, Morelli G, Novellino E, Marasco D (2017). Insights into amyloid-like aggregation of H2 region of the C-terminal domain of nucleophosmin. Biochim Biophys Acta 1865, 176–185.

Sagawa F, Ibrahim H, Morrison AL, Wilusz CJ, Wilusz J (2011). Nucleophosmin deposition during mRNA 3′ end processing influences poly(A) tail length. EMBO J 30, 3994–4005.

Samejima K, Platani M, Wolny M, Ogawa H, Vargiu G, Knight PJ, Peckham M, Earnshaw WC (2015). The inner centromere protein (INCENP) coil is a single α-helix (SAH) domain that binds directly to microtubules and is important for chromosome passenger complex (CPC) localization and function in mitosis. J Biol Chem 290, 21460–21472.

Sampath SC, Ohi R, Leismann O, Salic A, Pozniakovski A, Funabiki H (2004). The chromosomal passenger complex is required for chromatin-induced microtubule stabilization and spindle assembly. Cell 118, 187–202.

Scaloni F, Federici L, Brunori M, Gianni S (2010). Deciphering the folding transition state structure and denatured state properties of nucleophosmin C-terminal domain. Proc Natl Acad Sci USA 107, 5447–5452.

Scaloni F, Gianni S, Federici L, Falini B, Brunori M (2009). Folding mechanism of the C-terminal domain of nucleophosmin: residual structure in the denatured state and its pathophysiological significance. FASEB J 23, 2360–2365.

Scognamiglio PL, Di Natale C, Leone M, Poletto M, Vitagliano L, Tell G, Marasco D (2014). G-quadruplex DNA recognition by nucleophosmin: new insights from protein dissection. Biochim Biophys Acta 1840, 2050–2059.

Sessa F, Mapelli M, Ciferri C, Tarricone C, Areces LB, Schneider TR, Stukenberg PT, Musacchio A (2005). Mechanism of Aurora B activation by INCENP and inhibition by hesperadin. Mol Cell 18, 379–391.

Sessa F, Villa F (2014). Structure of Aurora B-INCENP in complex with barasertib reveals a potential transinhibitory mechanism. Acta Crystallogr F Struct Biol Commun 70, 294–298.

Shalloway D, Taylor SJ (1997). Src: more than the sum of its parts. Trends Cell Biol 7, 215–217.

Shandilya J, Senapati P, Dhanasekaran K, Bangalore SS, Kumar M, Hari Kishore A, Bhat A, Kodaganur GS, Kundu TK (2014). Phosphorylation of multifunctional nucleolar protein nucleophosmin (NPM1) by aurora kinase B is critical for mitotic progression. FEBS Lett 588, 2198–2205.

So CH, Michal AM, Mashayekhi R, Benovic JL (2012). G protein-coupled receptor kinase 5 phosphorylates nucleophosmin and regulates cell sensitivity to polo-like kinase 1 inhibition. J Biol Chem 287, 17088–17099.

Staus DP, Taylor JM, Mack CP (2011). Enhancement of mDia2 activity by Rho-kinase-dependent phosphorylation of the diaphanous autoregulatory domain. Biochem J 439, 57–65.

Szebeni A, Olson MOJ (1999). Nucleolar protein B23 has molecular chaperone activities. Protein Sci 8, 905–912.

Tseng BS, Tan L, Kapoor TM, Funabiki H (2010). Dual detection of chromosomes and microtubules by the chromosomal passenger complex drives spindle assembly. Dev Cell 18, 903–912.

Wilczek C, Chitta R, Woo E, Shabanowitz J, Chait BT, Hunt DF, Shechter D (2011). Protein arginine methyltransferase Prmt5-Mep50 methylates histones H2A and H4 and the histone chaperone nucleoplasmin in Xenopus laevis eggs. J Biol Chem 286, 42221–42231.

Wuhr M, Freeman RM Jr, Presler M, Horb ME, Peshkin L, Gygi SP, Kirschner MW (2014). Deep proteomics of the Xenopus laevis egg using an mRNA-derived reference database. Curr Biol 24, 1467–1475.

Wuhr M, Guttler T, Peshkin L, McAlister GC, Sonnett M, Ishihara K, Groen AC, Presler M, Erickson BK, Mitchison TJ, *et al.* (2015). The nuclear proteome of a vertebrate. Curr Biol 25, 2663–2671.

Yasui Y, Urano T, Kawajiri A, Nagata K-i, Tatsuka M, Saya H, Furukawa K, Takahashi T, Izawa I, Inagaki M (2004). Autophosphorylation of a newly identified site of Aurora-B is indispensable for cytokinesis. J Biol Chem 279, 12997–13003.